Journal of
Manufacturing and Materials Processing

MDPI

Article

Microstructure and Thermal Mechanical Behavior of Arc-Welded Aluminum Alloy 6061-T6

Zeli Arhumah and Xuan-Tan Pham *

Department of Mechanical Engineering, École de Technologie Supérieure, 1100, Rue Notre-Dame West, Montreal, QC H3C 1K3, Canada; zeli.alhur@gmail.com
* Correspondence: tan.pham@etsmtl.ca

Abstract: In this study, the welding thermal cycle, as well as the microstructural and mechanical properties of welded AA6061-T6 plates, were studied. The plates were prepared and bead-on-plate welded using gas metal arc welding (GMAW). Numerical simulations using SYSWELD® were performed to obtain the thermal distribution in the welded plates. The numerical heat source was calibrated using the temperatures obtained from the experimental work and the geometry of the melting pool. The mechanical properties were obtained through microhardness tests and were correlated with the welding thermal cycle. Moreover, the mechanical behavior and local deformation in the heat-affected zone (HAZ) were investigated using micro-flat tensile (MFT) tests with digital image correlation (DIC). The mechanical properties of the subzones in the HAZ were then correlated with the welding thermal cycle and with the microstructure of the HAZ. It was observed that the welding thermal cycle produced microstructural variations across the HAZ, which significantly affected the mechanical behavior of the HAZ subzones. The results revealed that MFT tests with the DIC technique are an excellent tool for studying the local mechanical behavior change in AA6061-T6 welded parts due to the welding heat.

Keywords: aluminum welding; heat analysis; microstructure; mechanical behavior; finite element analysis

Citation: Arhumah, Z.; Pham, X.-T. Microstructure and Thermal Mechanical Behavior of Arc-Welded Aluminum Alloy 6061-T6. *J. Manuf. Mater. Process.* **2024**, *8*, 110. https://doi.org/10.3390/jmmp8030110

Academic Editor: Chao Yang

Received: 9 May 2024
Revised: 24 May 2024
Accepted: 24 May 2024
Published: 26 May 2024

1. Introduction

Aluminum alloys have many favorable properties, which have led to their widespread use; indeed, today, they collectively rank as the second most used metal in manufacturing after steel [1]. Aluminum alloy AA6061-T6 (Al-Si-Mg) is heavily used in industries such as aerospace, automobile, aeronautic, and construction, just to name a few. It derives its properties from the formation of the Mg_2Si intermetallic precipitated β'' phase, which is metastable and coherent with the matrix [2,3]. In the welding process, phase transformation may occur under the welding heat due to the instability of this phase [4–7].

Welding is one of the most efficient and practical metal joining processes. Arc welding processes are widely used for AA6061 alloys. Despite its many advantages, fusion welding presents several limitations. Welding thermal cycles significantly affect the mechanical properties and microstructure of the heat-affected zone (HAZ) [8–12]. Because the mechanical behavior and the final microstructure of weldments are mainly a function of the welding thermal cycle [7,13–16], the latter must be investigated and correctly predicted. Walter et al. [14] attributed the variation in hardness across the HAZ and in the tensile properties in different welding processes to microstructural variations. Gómora et al. [17] reported observing a low hardness subzone within the HAZ, with optical microscopy indicating no apparent significant grain size changes in this subzone.

Accurately capturing the thermal profile in the HAZ during welding, particularly fusion welding, is essential to understanding how the welding heat relates to the microstructure and mechanical properties of the material; however, this is made challenging by the

inherently harsh welding atmosphere [18,19]. The welding arc generates high temperatures, which is its main characteristic, but it also produces various secondary effects, such as electromagnetic fields, spatter, and radiation. Lee et al. [20] studied the microstructural change triggered by the peak temperature and cooling rate during gas tungsten arc welding. The thermal profile was recorded at different locations in the HAZ and base metal; additionally, the thermal history was correlated to the material's microstructure in order to understand the changes introduced by specific thermal profiles.

Many authors [13,20–25] investigated the thermal profile in an AA6061-T6 welded specimen using numerical simulations to evaluate the heat effect on the mechanical behavior of the weld joint. It was found that finite element analysis (FEA) could be used to optimize the welding process parameters with a reduced number of experiments. The following numerical analyses of aluminum welding were carried out using SYSWELD 2019®, a special finite element software for heat treatment and welding. Francis [21] optimized the welding process of aluminum 2519-T87 T-joint for reducing residual stresses. Nazemi [22] numerically investigated the welding thermal cycle of an AA6061-T6 T-joint and predicted a mechanical strength reduction in the HAZ versus the base metal. Nélias et al. [25] analyzed the metallurgical transformation caused by the thermal cycle during the laser welding of AA6056-T4.

Various studies have reported the effects of variations in the welding thermal cycle on local mechanical properties across the HAZ [5,16]. In [26–28], Digital Image Correlation (DIC) was used to characterize the heterogeneous subzones in the HAZ. Lockwood et al. [29] numerically and experimentally examined the local mechanical properties of Friction Stir Welding (FSW) on an aluminum alloy AA2024 joint. In their study, local strain measurements were performed on flat tensile samples using the DIC method.

This present study investigated the relation between the welding heat, the mechanical behavior, and the microstructure of AA6061-T6 arc-welded plates. Particular attention was paid to the welding thermal cycle in the HAZs, which results in a complex microstructure. The local mechanical behavior of the HAZ was documented using digital image correlation, which revealed that the welding thermal cycle has a strong effect on the microstructure of the HAZ. Different HAZ subzones were also observed in detail in order to determine the relation between the thermal cycle and the local mechanical properties of the AA6061-T6 welded plates. The local strains in these HAZ subzones were also observed with the DIC technique until the necking.

2. Materials and Methods

2.1. Material Used and Welding Procedure

AA6061-T6 aluminum alloy (Al-Si-Mg) plates measuring 205 mm × 50 mm × 6 mm were prepared for the welding process. A 1.2 mm diameter filler wire ER4043 (Al-Si) was used. The nominal chemical composition of the filler metal (FW) and base metal (BM) are listed in Table 1.

Table 1. Chemical composition of materials (wt %).

	Al	Cr	Cu	Fe	Mn	Mg	Si	Ti	Zn
BM (AA6061-T6)	98.6	0.004	0.15	0.7	0.15	0.8	0.4	0.15	0.25
FW (ER4043)	93.3	---	0.3	0.8	0.05	0.05	5.25	0.2	0.1

A DX-100 Yaskawa robot integrated with a standard Fronius Trans Plus Synergic 4000 GMAW power supply was used for this investigation. The flexibility of robotic welding operations means that a steadier weld quality can be achieved with fewer defects. The welding parameters used in this study are illustrated in Table 2. With the welding current I, voltage V, and thermal efficiency η, the heat generated during welding was calculated as follows:

$$Q = \eta IV \quad (1)$$

Table 2. Welding parameters.

Wire Feeding Speed (mm/s)	Voltage (V)	Ampere (A)	Welding Speed (mm/s)	Angle (Degree)	Shield Gas (Argon) (L/min)
114.2	23.2	174	15.2	15°	12

The GRAPHTECH GL220A data acquisition system and type K thermocouples fabricated with Alumel and Chromel materials with a diameter of 0.5 mm were used to measure the temperature. The data acquisition rate was 10 readings per second from each thermocouple. The thermocouples were installed using a TW163/V Variable Energy Thermocouple Welding Unit. Eight thermocouples were installed, with four on each side of the welding line. Figure 1 shows the distance of each thermocouple from the welding line. Ceramic tubes were used to separate the thermocouple wires and to protect the thermocouples from splatter.

Thermocouple	X(mm)	Y(mm)
TC1	100	5
TC2	100	7
TC3	100	9
TC4	100	11
TC5	100	–5
TC6	100	–7
TC7	100	–9
TC8	100	–11

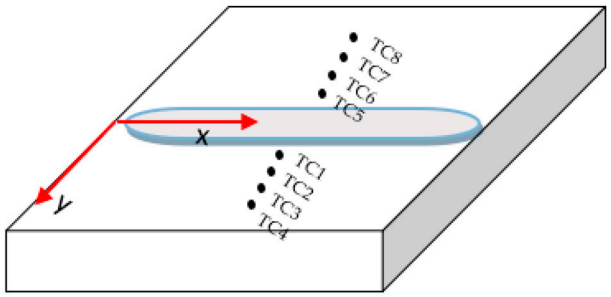

Figure 1. Location of thermocouples installed on the plate (TC1 to TC8).

2.2. Numerical Procedure

SYSWELD 2019® is a commercial finite element software package designed by the ESI Group specifically for welding and heat treatment process simulation [30]. It was used in this study to predict the distribution of the temperature in the weldment.

A three-dimensional conical Gaussian heat source, presented in Figure 2, was applied to simulate the welding thermal cycle during a bead-on-plate welding pass as indicated in Figure 3a. The parameters of this heat source are shown in Table 3, where Q_0 is the heat density, r_i, and r_e are the radius of the heat source at the position z_i and z_e, respectively, and Q_{eff} is the effective power. For more details about this heat source, please refer to reference [30]. The material's mechanical properties at room temperature for base material (BM) and filler wire (FW) are presented in Table 4. The dimensions in the simulation model were the same as those of the experimental plates. The geometric model of the welded plate was meshed. A fine mesh was used in the fusion zone and its adjacent, as shown in Figure 3b. The irregular mesh size was chosen following a peak temperature sensitivity analysis with an exactitude of around a 1.7% difference in the peak temperatures. The initial temperature of the plate is 20 °C. The exterior surface of the plate is applied with natural convection as a boundary condition with the convection heat transfer coefficient of 25 W/(m^2·K). The temperature of the room is also 20 °C.

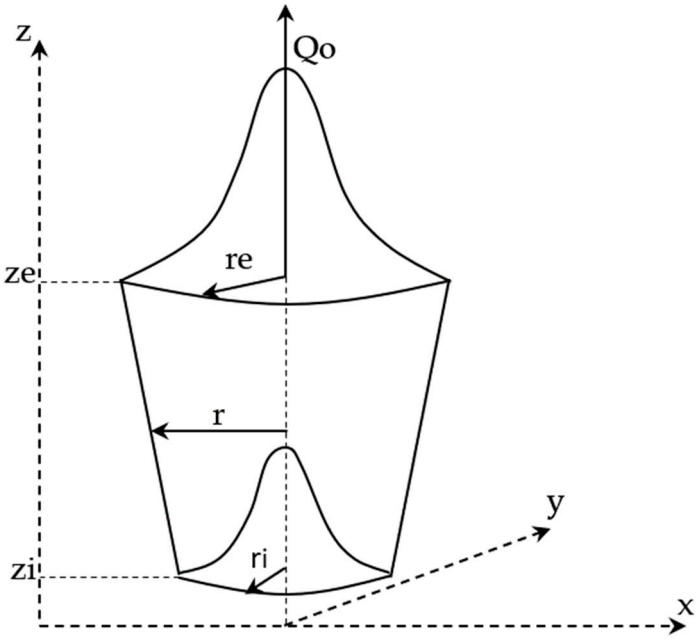

Figure 2. Conical Gaussian volumetric heat source model.

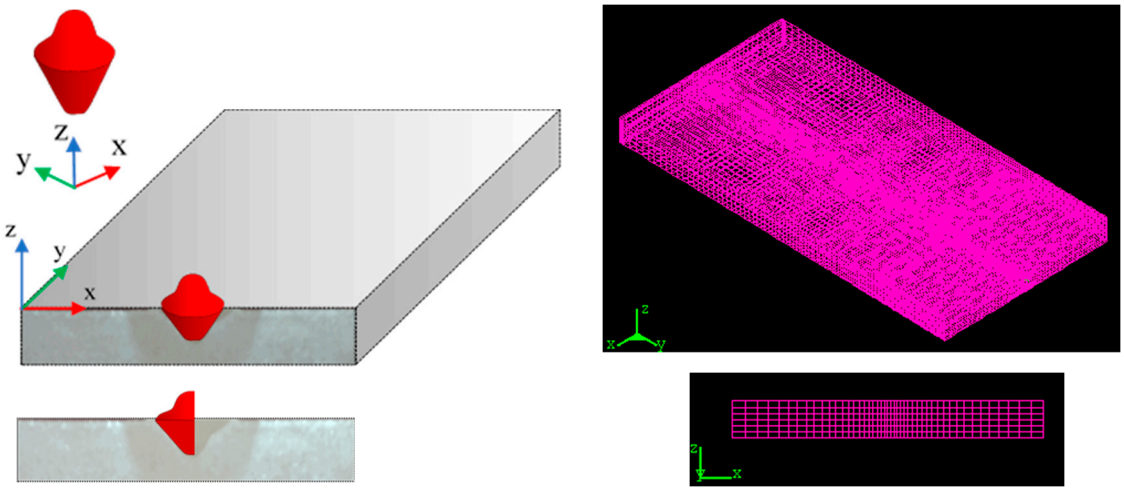

(**a**) (**b**)

Figure 3. Mesh used for numerical simulations using Sysweld: (**a**) application of the heat source, (**b**) irregular mesh.

Table 3. Three-dimensional conical heat source parameters.

Welding Speed (mm/s)	Q_0 (W/mm^3)	r_e (mm)	z_e (mm)	r_i (mm)	z_i	Q_{eff} (W)
15.2	32.7	6	3	4	1	3150

Table 4. Material's mechanical properties (nominal values).

Type of Material	YS (MPa)	UTS (MPa)	Elongation (%)	Hardness (Vickers)
BM (AA6061-T6)	276	310	12	107
FW (ER4043)	70	145	22	47

2.3. Samples' Preparation for Microstructure Characterization

Specimens of a cross-section perpendicular to the welding line were prepared. The sample was sectioned with a META-CUT water-cooled abrasive cutter (Metkon USA, Inc., Mauldin, SC, USA), and the first 30 mm of the weldment was discarded to avoid unsteady state conditions. Next, the specimens were mounted and polished using a NANO 2000T polishing machine (PACE Technologies, Tucson, AZ, USA) and using different grades of silicon carbide paper, ranging from 400 up to 2400 grit. Finally, they were finished by using 3 µm, 1 µm, and 0.05 µm size polishing pads.

To prepare the specimens for optical microscopy, samples were etched with caustic sodium fluoride (93 mL water, 2 g NaOH, 5 g NaF). The specimens were examined with an Olympus Lext 4100 light microscope (Olympus America) to isolate any defects present and to identify the main microstructural characteristics of the GMAW in the base metal (BM), the partially melted zone (PMZ), the heat-affected zone (HAZ), and the fusion zone (FZ).

2.4. Microhardness Measurement

Microhardness measurements were carried out on the mounted specimens at room temperature on a cross-section perpendicular to the welding line to cover all zones affected by the thermal cycle. An automatic microhardness Clemex CMT (Clemex Technologies Inc., Brossard, QC, Canada) was used to measure the hardness. A dwell time of 15 s and a load of 100 g were used, in accordance with the ASTM E92 standard procedure for the Vickers hardness test of Metallic Materials.

The parameters were kept constant for all indentations, with a 150 µm maintained distance between the indentations. The microhardness measurements were analyzed as a function of peak temperature and distance from the welding centerline. A 2D map was generated to cover all zones in the cross-section and to investigate the hardness distribution.

2.5. Micro-Flat-Tensile Tests with Digital Imaging Correlation

Micro-flat-tensile (MFT) specimens were extracted from welded samples and used in this investigation. A schematic diagram of the traction samples is shown in Figure 4. First, dog-bone sub-size traction samples were extracted from the welded sample normal to the welding line direction using a CNC machine as presented in Figure 4a. Figure 4b shows the cutting arrangement for the machined samples. A 24 mm gauge length was selected to cover different zones in the sample, such as the BM, HAZ, PMZ, and FZ, as shown in Figure 4c,d. The extracted samples were approximately 1 mm thick (±0.02), and care was taken to avoid any deformation or sequencing errors.

Traction tests were carried out using a 5 kN micro-tensile (Kammrath and Weise GmbH, Schwerte, Germany) machine under crosshead velocity control (2.1×10^{-4} s^{-1}). The crosshead displacement was documented frequently, with a 1 µm accuracy, and a non-contact laser extensometer was used to measure the elongation during the tests. A high-resolution camera was used to record images (1 image per second) during the tensile tests. GOM 2019 correlation software was used to calculate the in-plane displacement [31]. The displacement calculated from image correlation was used to obtain the in-plane local strain field.

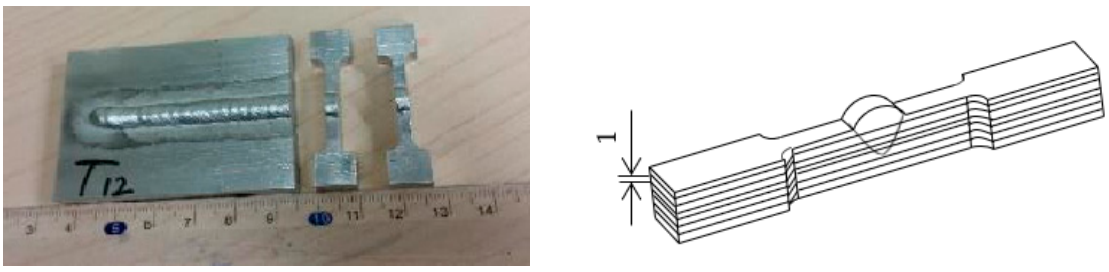

(**a**) (**b**)

Figure 4. *Cont.*

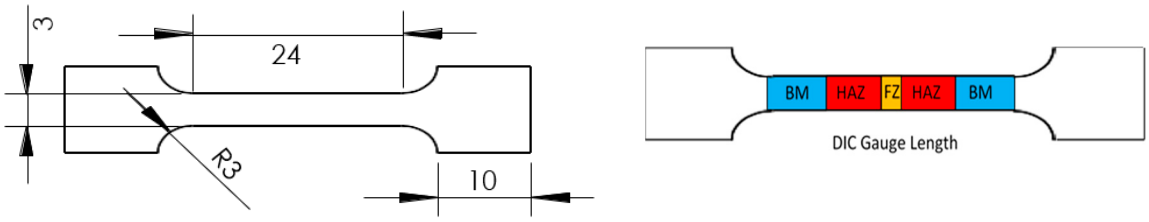

(**c**) (**d**)

Figure 4. MFT specimen: (**a**) machined samples, (**b**,**c**) extracted micro-tensile specimen (dimensions in mm), and (**d**) regions of interest extracted from the welded sample used for DIC.

3. Results and Discussions

3.1. Thermal Profile and Melting Zone

Figure 5 shows the temperature distribution and melting zone calculated by finite element analysis (FEA) using Sysweld (right side) and compared with the experimental results (left side). From the experimental and FEA thermal profile distribution, zones can be classified as base material, heat-affected zone, and fusion zone. It is clear that the melted zone calculated by FEA matches the experimental melting zone size, with slight differences resulting from the addition of filler.

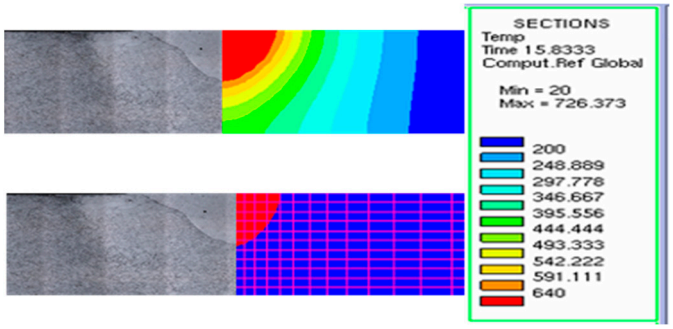

Figure 5. Melting zone experimental results compared with FEA.

Figure 6a compares the welding thermal profiles obtained by K-type thermocouples in four different locations measured from the welding line with numerical results. These results are generally in very good agreement; however, at peak temperatures, slight differences were observed, with the differences increasing with a decrease in the distance from the welding line. This is probably attributable to the effect of shielding gas and molten spattering of filler wire during fusion welding. Table 5 and Figure 6b present the comparison in peak temperatures transverse to the welding line. It is worth noting that the peak temperature variation has a nonlinear relationship with distance from the welding line.

Table 5. Differences in peak temperatures.

	Peak Temperature °C			
Thermocouples	TC1	TC2	TC3	TC4
Experimental	453	331	276	246
FEA	424	316	266	239.8
Difference	6.4%	4.5%	3.1%	2.5%

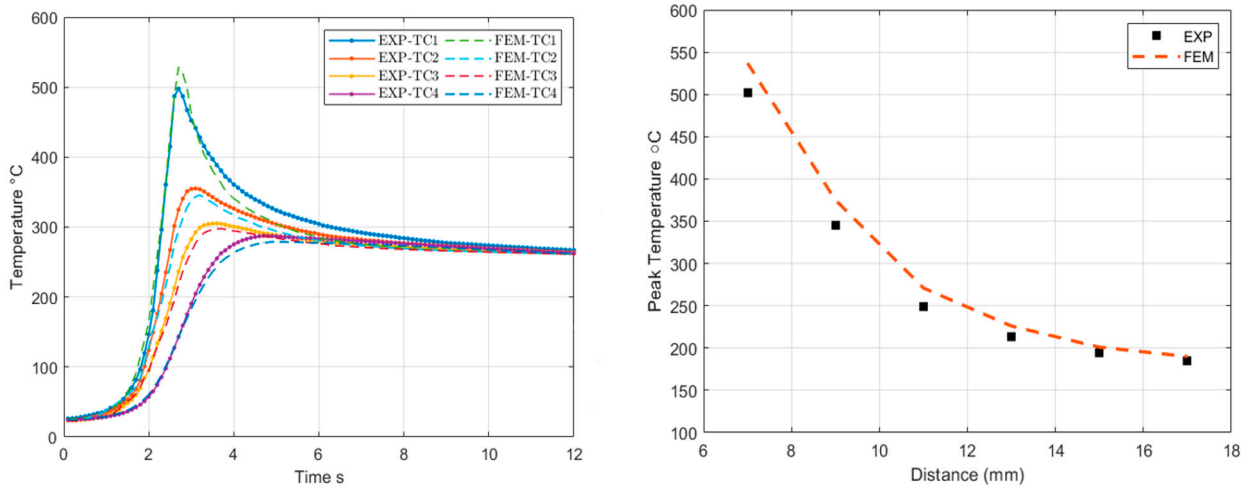

(**a**) (**b**)

Figure 6. Thermal profile: (**a**) comparison between experiments and finite element simulation at points at different distances from the welding center line; (**b**) peak temperature comparison.

3.2. Microstructure

In the present study, light optical photomicrographs were taken with different magnifications to study the microstructure variation across different zones such as the FZ, subzones of the HAZ, and the BM.

The microstructure of the base metal AA6061 in the T6 condition is shown in Figure 7. A polished and unetched sample, presented in Figure 7a, shows a nonuniform distribution of intermetallic particles throughout the microstructure of the base metal. However, the etched sample in Figure 7b shows the grains of the base metal and the grain boundaries which appear as a thick, dark, etched layer. The base metal has a mean equiaxed grain size of around 43 µm.

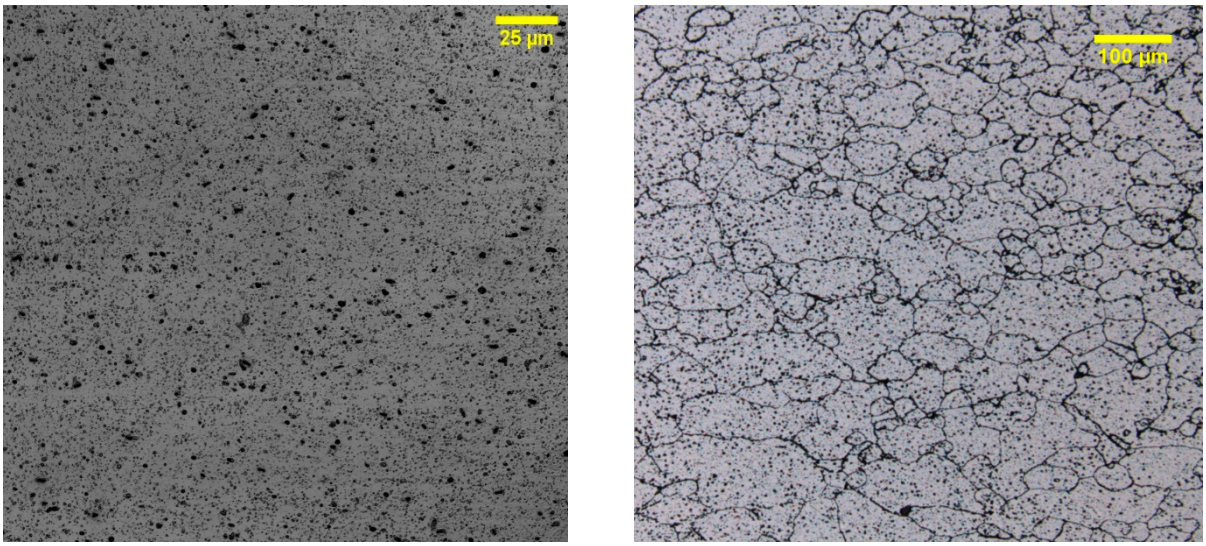

(**a**) (**b**)

Figure 7. Base metal of AA6061-T6: (**a**) coarse second phase particles distributed randomly; (**b**) grain size of base metal.

The as-welded condition of AA6061-T6 shows a well-defined grain boundary in the fusion zone (FZ), as indicated in Figure 8a. The FZ consists of small grains of varying

shapes that range from 10 µm to 20 µm. The columnar grains are found in FZ at the interface with the HAZ. Meanwhile, the center of the welded metal was solidified into equiaxed grains. There is a clear difference in microstructure between the FZ and the HAZ, as shown in Figure 8b.

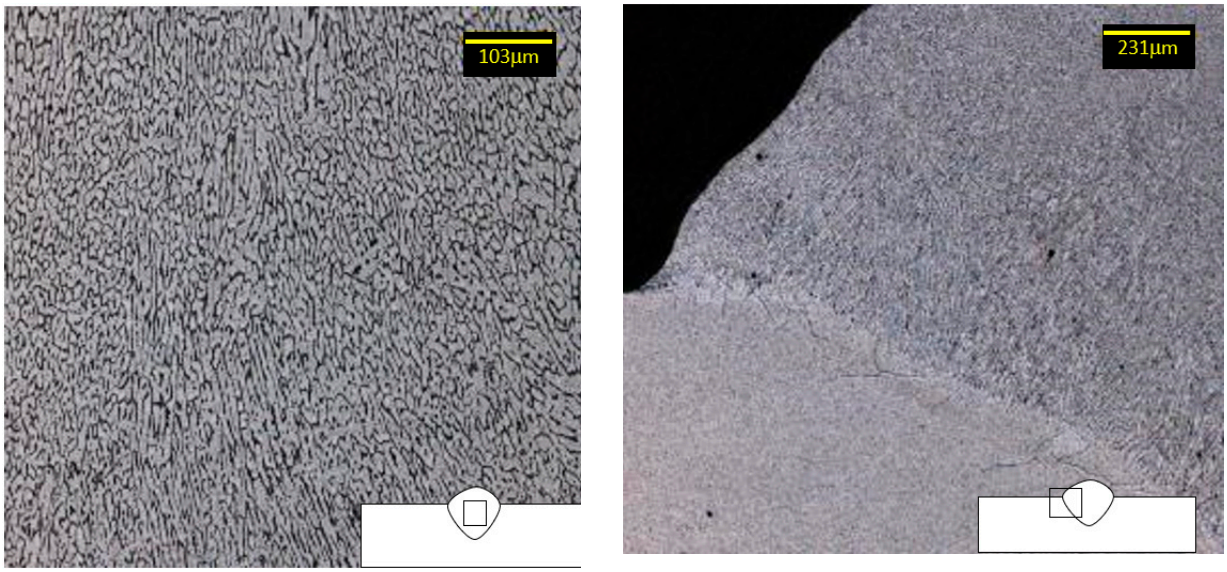

(**a**) (**b**)

Figure 8. Light optical micrographs of microstructure of FZ and HAZ: (**a**) grains in FZ; (**b**) interface between the HAZ and fusion zone FZ.

Figure 9a shows grains in the HAZ adjacent to the FZ, where the average grain size is around 318 µm. It was also observed that the grain size beneath the fusion zone decreases gradually as a function of distance from the welding line, as depicted in Figure 9b. Grain growth has a proportional relationship with peak temperature in terms of exposure time. However, its effect on mechanical properties compared with the effect of precipitation transformation is not significant [32,33], as can be observed by comparing the grain size with the lowest hardness in HAZ, which will be discussed in more detail in the next section.

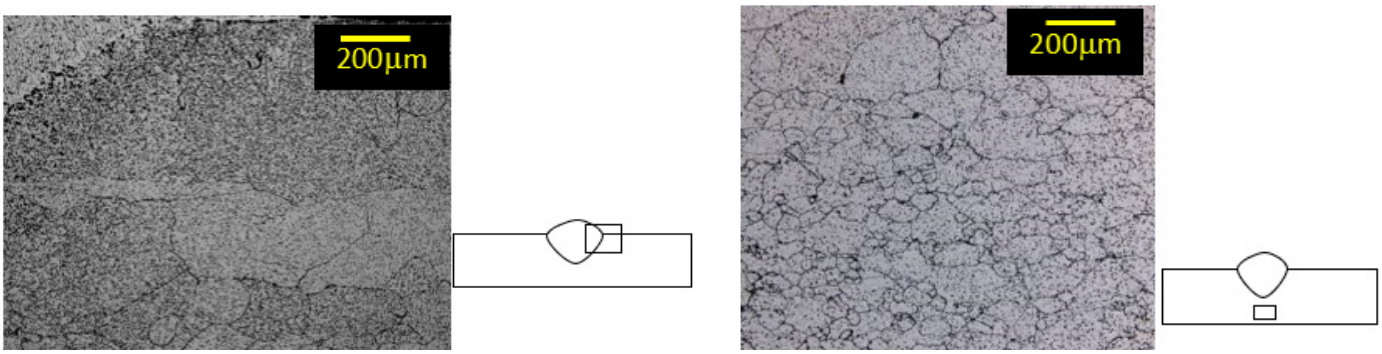

(**a**) (**b**)

Figure 9. Light optical micrographs of recrystallization and grain growth: (**a**) zone adjacent to FZ; (**b**) gradual change in grain size in the zone beneath the FZ.

3.3. Microhardness across the HAZ

Figure 10 illustrates the profile of the maximal temperatures (T_{MAX}), with microhardness results overlapping one another. By examining the relationship between the T_{MAX} and hardness, it can be seen that the FZ, which was exposed to T_{MAX} over 652 °C, has a

low average hardness value of 73 HV, which could be attributed to a lack of precipitates, a change in chemical composition, and the porosity present in this zone. As observed in Figure 10, three HAZs can be distinguished, namely, HAZ1, HAZ2, and HAZ3. The zone HAZ1 adjacent to the FZ was subjected to peak temperatures between 380 °C and 560 °C and has an average hardness value of 80 HV. Here, the precipitates of β″ dissolved or transformed to β′ (with respect to the distance from the FZ boundary), and the material became a combination of α + β′ phases, as explained in [34–36]. The natural aging in this zone increased the hardness to 80 HV. The plane separating HAZ1 from HAZ2 was subjected to a critical temperature ranging from 290 °C to 380 °C. It had the highest β′ phase fraction because the critical temperature led to the dissolution of needle-shaped fine precipitates of β″, and the biggest one started to grow and form a rod shape β′, as presented in [34–36]. This plane had the lowest hardness value of 70 HV. Zone HAZ3 was exposed to a peak temperature ranging from 290 °C down to 190 °C, and its hardness value gradually increased to match that of the base metal. At less than 190 °C, the material was not affected by the welding thermal cycle.

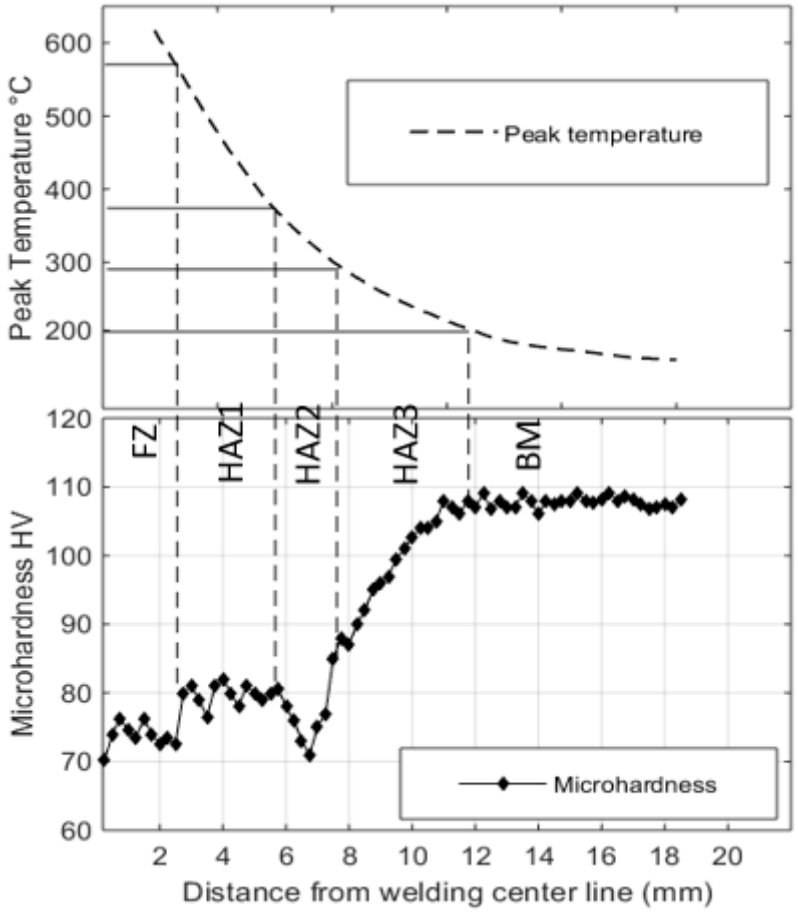

Figure 10. Correlation between thermal cycle and microhardness values in HAZ.

3.4. Micro-Flat-Tensile Tests Using DIC

Figure 11 and Table 6 present a comparison of our experimental results of the stress–strain curves as the mechanical behavior of the base metal and welded specimens.

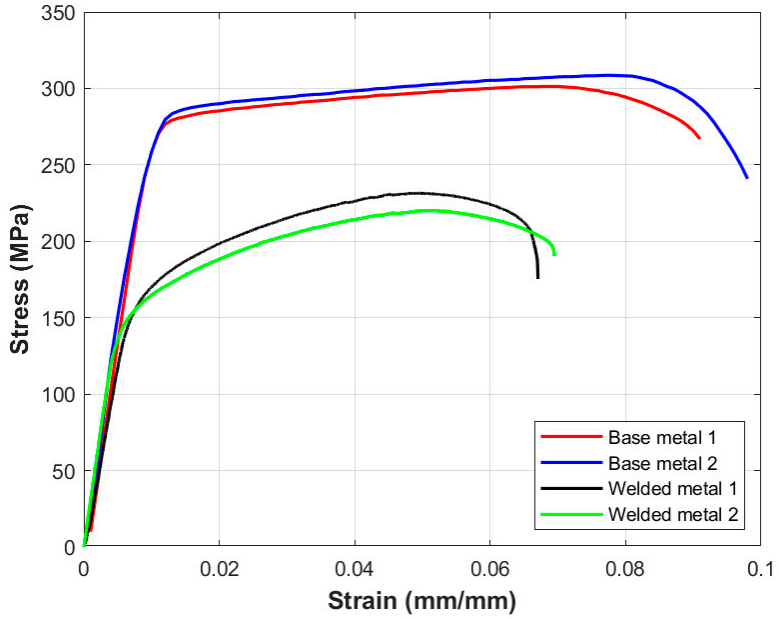

Figure 11. Global response (stress–strain) curves for welded sample and parent metal.

Table 6. Mechanical properties of base and welded metals.

	Welded Metal			Base Metal		
Description	Test 1	Test 2	Ave.	Test1	Test2	Ave.
Yield Stress (MPa)	153	162	157.3	271	271	274
Ultimate strength (MPa)	220	231	226	301	308	305
Elongation (%)	6.8	6.7	6.8	9.1	9.8	9.4

The plastic strains of 0.2% at the yield strength (YS) and 4.4% at the ultimate tensile strength (UTS) were found in the welded samples. The stress gradually decreased as the strain exceeded the UTS zone, and as a result of substantial necking at approximately 6.5 mm from the welding line, the samples finally fractured at 6.8% strain.

3.4.1. Local Behavior of HAZ Subzones in Welded Plate Obtained by DIC

The sample depicted in Figure 12 represents the deformation measured with DIC in the x (longitudinal) and y (transversal) directions. Two tests were performed. The results of these tests are coherent and show that the local in-plane strains obtained from DIC can be used for local strain analysis.

Strain measurements were captured at four stages (in elastic and plastic) of loading by DIC, and the results are illustrated for both directions in Figure 12. The stages correspond to the principal stress level in the x-direction and the mean strain values. It is noted that the strain was initially evenly distributed across the gauge length (FZ and HAZ) until the stress reached 126 MPa, as shown in Figure 12.

The three stages, as depicted in Figures 12 and 13, represent the mean local strain values measured with DIC. The ε_{xx} and ε_{yy} strain fields correspond to the x- and y-axes, namely, the cross-welding and the welding direction, respectively. The average values of ε_{xx} and ε_{yy} for the regions of interest on both sides of the weld center line are plotted as a function of the cross-weld direction for different strain levels. The overall deformation is not distributed evenly and shows different behaviors across the FZ, HAZ, and BM. In Stage 1, at a stress value of 180 MPa, the strain starts to concentrate at approximately 6.5 mm from the welding line on both sides of the weld. In Stage 2, an increase in stress value up to 213 MPa leads to a strain concentration in the two planes (named PZ1 and PZ2). Finally,

in Stage 3, when the stress value approaches the UTS value (221 MPa), necking begins to occur at one of these two planes before fracture.

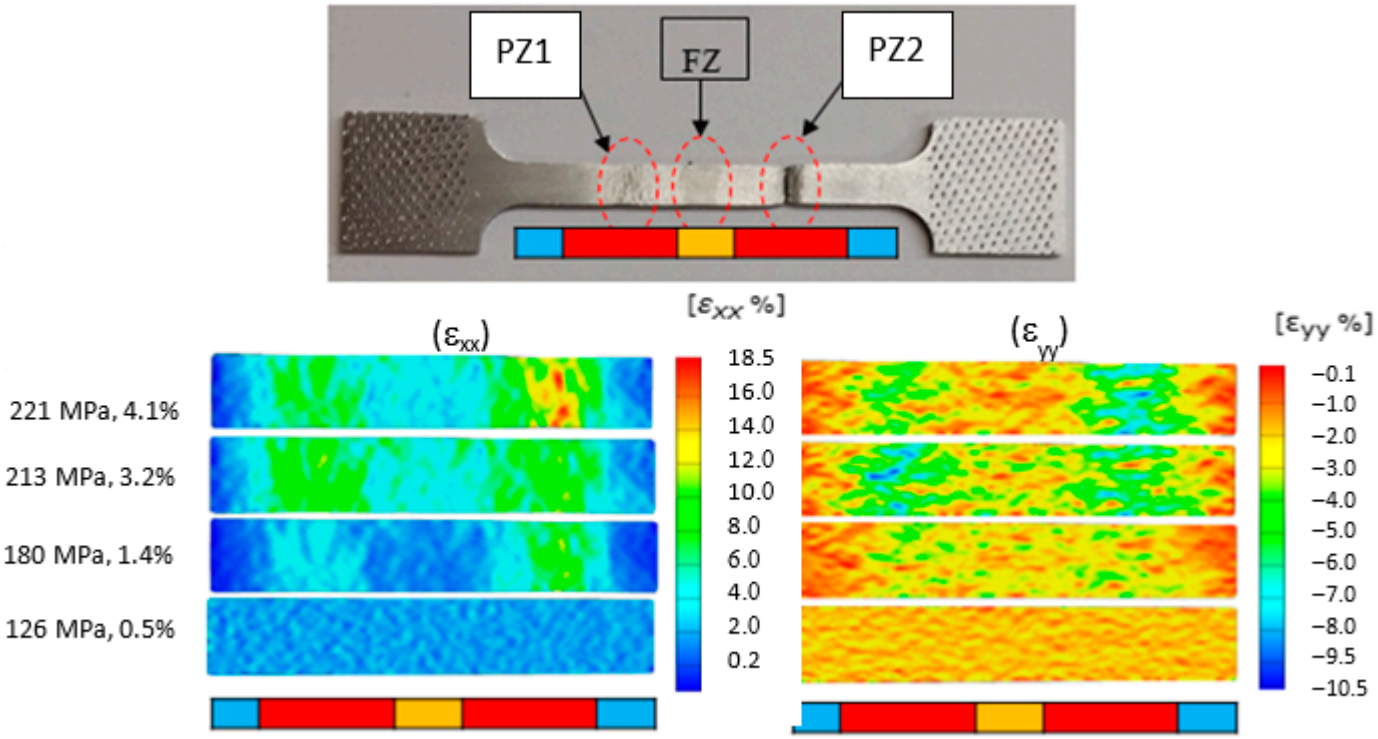

Figure 12. Illustration of the distribution of local in-plane strain acquired using DIC equivalent to different strains (corresponding to 24 mm specimen gauge length) for two specimens.

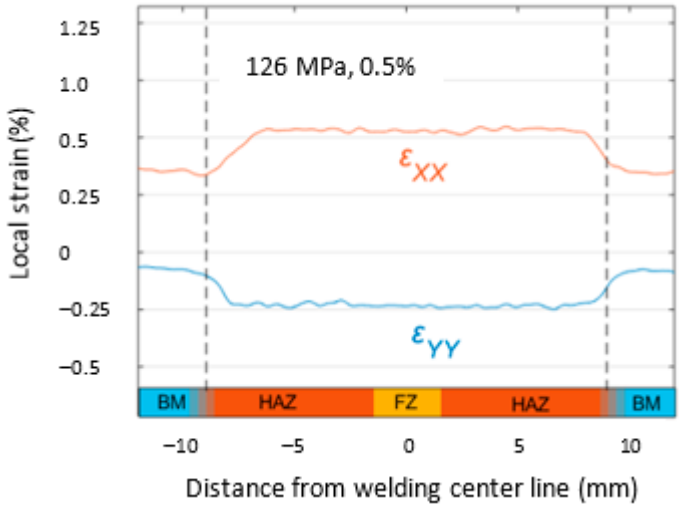

(**a**)

Figure 13. *Cont.*

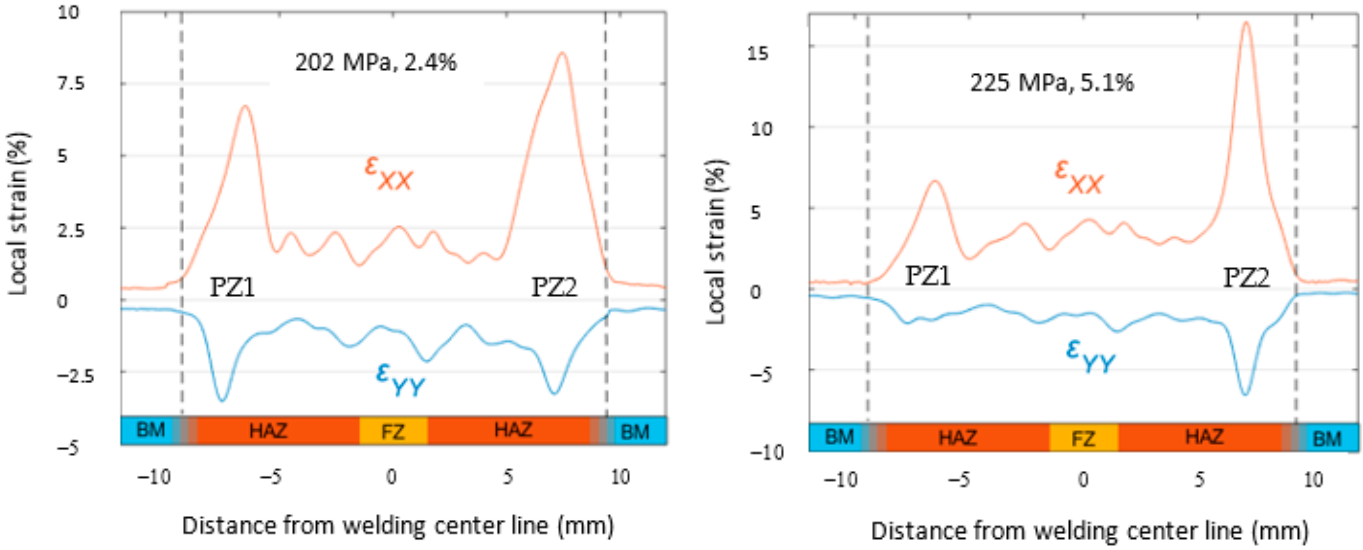

(**b**) (**c**)

Figure 13. Average value of ε_{XX} and ε_{YY} in transverse weld direction for three stress/strain stages: (**a**) 126 MPa_0.5%; (**b**) 202 MPa_2.4%; and (**c**) 225 MPa_5.1%, illustrating local in-plane strain localization.

At the first stage of deformation (126 MPa—0.5%), the ε_{xx} strain fields exhibit an equal strain distribution across the softened zone (FZ and HAZ, 9.5 mm from the welding center line on both sides). At this stage, the variation in local strain is only 0.25% between the soft zone and the BM, as presented in Figure 13a. Increasing the load value (180 MPa—1.4%) reveals a strain concentration in the plane at 6.5 mm from the welding line on both sides of the welding center line. The strain value reaches an average of 8.5% at the high deformation plane (softest plane across the HAZ) compared to 2.5% in the FZ and 0.35% in the BM, as shown in Figure 13b.

In the stage preceding necking (225 MPa—5.1%), the local deformation is mainly located 6.5 mm from the welding center line in one of the high deformation planes (PZ1 and PZ2), until the strain reaches 16% (PZ2) compared to another plane, which reaches 7% (PZ1). The mean strain value of the FZ and HAZ, excluding the softest plane, is around 5%, which is 30% of that found in the highly deformed plane. The local strain increases in this plane until fracture, as shown in Figure 13c. Interestingly, the ε_{xx} response remains approximately at the same value along the soft zone, with respect to each stage, except for the high deformation plane, which suffers a high deformation during the necking stage.

3.4.2. Local Stress–Strain Properties Obtained Using DIC test

Assuming uniform stress, every local position in the gauge length undergoes the same stress at any applied load. The local mechanical behavior has been investigated using DIC at eight positions (Z1 to Z8) along the gauge length from the fusion zone to the base metal. Z1 is 0 mm from the center line, Z2 1.5 mm, Z3 3 mm, Z4 4.5 mm, Z5 6 mm, Z6 7.5 mm, Z7 9 mm, and Z8 is in the BM zone. Figure 14 situates the local strain investigated in the different zones: the fusion zone, HAZ, and base metal.

Figure 15 presents a plot of uniform DIC stress-local strain measurements for eight positions (Z1 to Z8) along the gauge length. Z4 and Z5 experienced softening and have the highest strain value and lowest yield strength, respectively. Zones Z1, Z2, and Z3 show similar behaviors at lower strain levels compared to Z4 and Z5. Zones close to the BM (Z6 and Z7) show a higher yield strength and lower deformation. It is clear that Z8 (the base metal) is still in the elastic region. Figure 16 plots the global mechanical response of over-aged zones in terms of the longitudinal stress–strain of the samples. The stress–strain curves of the two softest planes in the HAZ (PZ1 and PZ2 in Figure 13), the welded metal, and the parent metal are illustrated in the same figure. The PZ1 plane shows the highest

local deformation, where fracturing finally occurs. At this moment, the localization of strain up to 18% was observed in the PZ2 region, as shown in this figure.

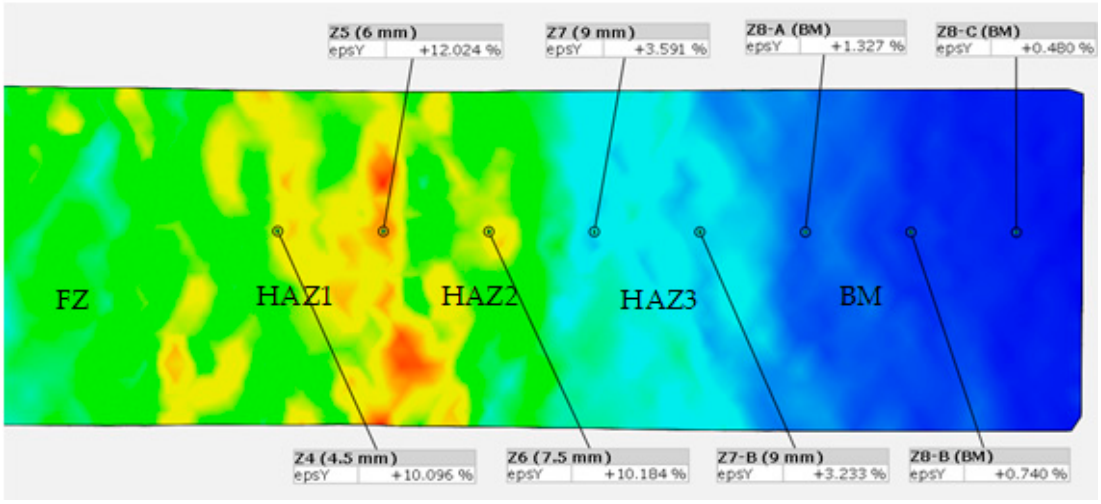

Figure 14. Different locations studied on the welded sample.

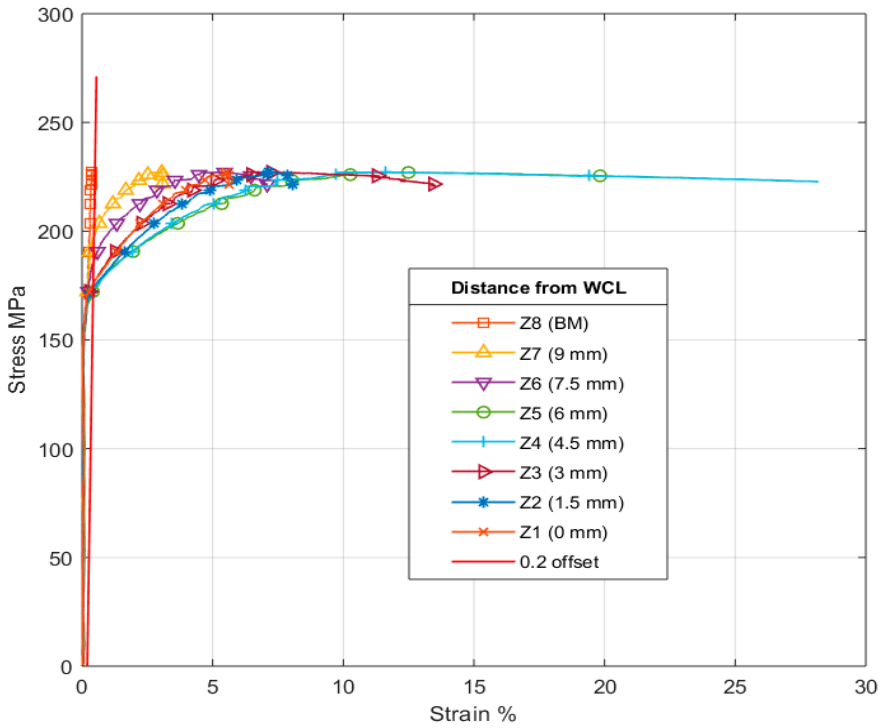

Figure 15. Stress-local strain in different locations obtained by DIC for welded sample.

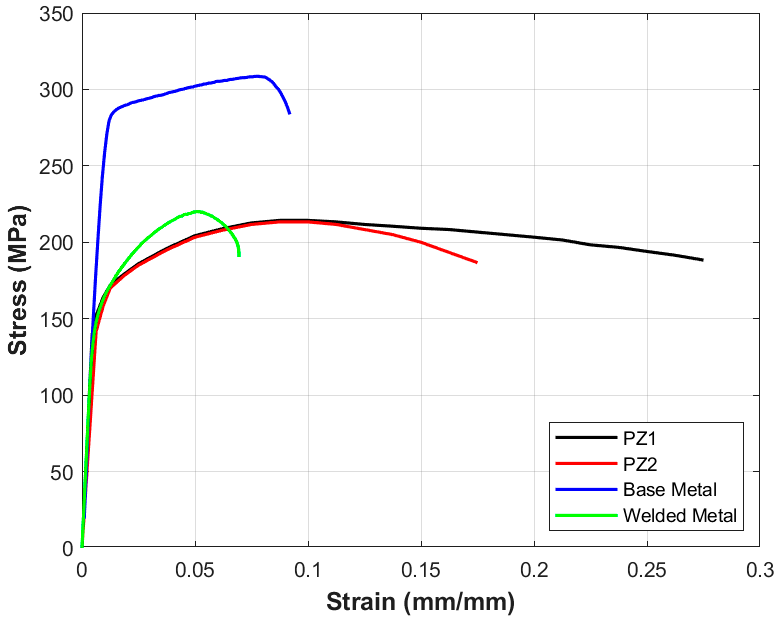

Figure 16. Average stress–strain behavior (DIC measurements) for welded joint and fracture planes in HAZ (PZ1 and PZ2) compared to base metal thermal cycle distribution across gauge length of DIC test specimen.

3.4.3. Thermal Profile and Mechanical Behavior

Figure 17 shows the welding thermal cycle distribution across the gauge length of the specimens extracted for the DIC. In the HAZ subzone adjacent to the FZ boundary, as explained in [34–36], where the peak temperature was between approximately 400 °C and 640 °C, the precipitate dissolved, resulting in the supersaturated solid solution (SSS), and because of the high cooling rate in this zone, which averaged −26 °C/s, the formation of re-precipitation during the cooling process was suppressed. In this zone, the increase in tensile properties could be attributed to the natural aging that occurs after cooling. The width of this subzone is about 4.1 mm.

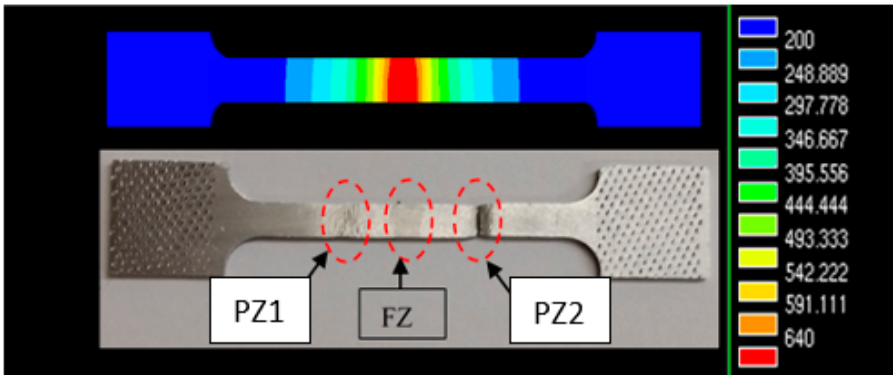

Figure 17. Historical temperature distribution (°C) of extracted samples for DIC tests.

The subzone was located approximately 5.9 mm from the welding center line, and extending to 8.1 mm, was exposed to a peak temperature of between 290 °C and 380 °C. In this over-aged zone, the temperature was not high enough to dissolve the precipitate to SSS; however, the temperature and slow cooling rate (6.4 °C/s) combination was enough to transform and coarsen the needle-shaped precipitate into a semi-coherent rod-shaped β' precipitate, causing the zone to undergo significant over-aging. The precipitate growth was the main factor causing softening in this zone. The local behavior obtained by DIC in this study is in good agreement with the microstructural analysis presented in [34–36].

Moreover, Figure 18 presents the measured microhardness of the DIC sample together with the historical temperature distribution and the microstructural analysis from [34–36]. This shows a very good agreement with the local strain analysis obtained in this present study.

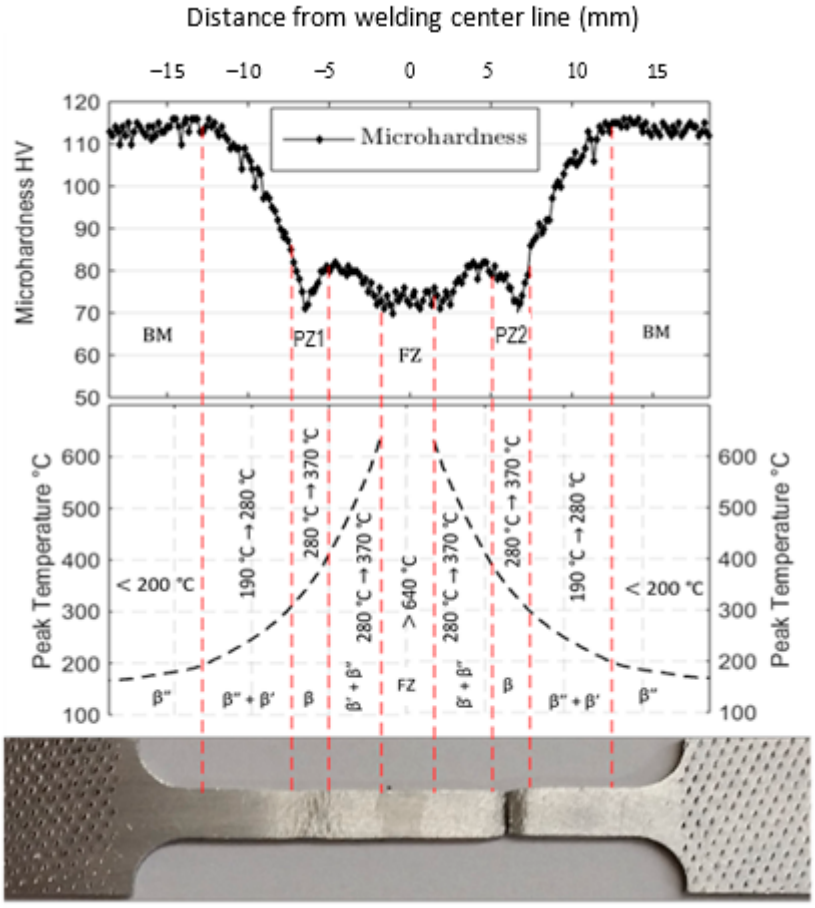

Figure 18. Correlations between mechanical properties and peak temperature profile along FZ and HAZ (Test-1 and Test-2).

4. Conclusions

The welding thermal profile, microstructure characterization, microhardness, and high-resolution digital image correlation (DIC) during tensile tests were used to document the local mechanical behavior of the HAZ in aluminum weldments obtained by a robotic GMAW process. The following conclusions can be drawn:

1. A thermal finite element analysis produced reasonably accurate results compared to the experimental thermal profile, and the most significant difference between the experimental results and the model results was an 8.3% difference in the temperature measured by the thermocouples nearest to the FZ.
2. The mechanical response of the welded sample was significantly influenced by the welding thermal cycle, and thermal cycle variations created different subzones in the HAZ. The over-aged subzone that produced the lowest hardness could be described as a 2.2 mm width plane located 5.9 mm to 8.1 mm on both sides of the welding center line. The symmetrical mechanical response on both sides of the weld was a result of the steady welding speed and robotic welding heat input.
3. The HAZ subzones present different plastic properties from zone to zone, and the local mechanical behavior of these zones varies according to the peak temperature to which they are exposed. The mechanical response of the heterogeneous HAZ led to the development of an extreme localization of deformed zones within which necking

and fracture occurred during tensile testing. These subzones were closely correlated with the peak temperature.

4. Micro-flat tensile tests using the DIC technique together with thermal numerical simulations provided a very interesting and powerful tool to understand the local mechanical behavior of the welded part. It revealed that welding heat is a crucial factor in the strength of AA6061-T6 weldment.
5. Although the microhardness technique was able to reveal the lowest hardness regions in the weldment, this technique has limitations when it comes to predicting the failure zone as it shows similar hardness values in the FZ and over-aged planes.

Author Contributions: Conceptualization, Z.A. and X.-T.P.; methodology, Z.A. and X.-T.P.; Experimental work, Z.A.; validation, Z.A. and X.-T.P.; investigation, Z.A.; resources, X.-T.P.; writing—original draft preparation, Z.A.; writing—review and editing, X.-T.P.; supervision, X.-T.P. All authors have read and agreed to the published version of the manuscript.

Funding: M. Zeli Arhumah has received a scholarship from the Libyan Ministry of Education for his master's project, through Canadian Bureau for International Eduction (CBIE), Dossier #2870.

Data Availability Statement: The datasets presented in this article are not totally readily available due to an ongoing study. Just some data presented in this study are available on request from the corresponding author.

Acknowledgments: X-T. Pham would like to thank the ESI group for the use of the software SYSWELD 2019 in this academic study and the Libyan Ministry of Education for providing M. Arhumah the opportunity to realize this project.

Conflicts of Interest: The authors declare no conflicts of interest.

References

1. Dursun, T.; Soutis, C. Recent developments in advanced aircraft aluminium alloys. *Mater. Des.* **2014**, *56*, 862–871. [CrossRef]
2. ASM International. Heat treating, Section "Heat treating of Aluminum Alloys". In *ASM International Handbook*; ASM International: Materials Park, OH, USA, 1991; Volume 4, p. 2173.
3. Buchanan, K.; Colas, K.; Ribis, J.; Lopez, A.; Garnier, J. Analysis of the metastable precipitates in peak-hardness aged Al-Mg-Si (-Cu) alloys with differing Si contents. *Acta Mater.* **2017**, *132*, 209–221. [CrossRef]
4. Easterling, K. *Introduction to the Physical Metallurgy of Welding*; Butterworth-Heinemann Ltd.: Oxford, UK, 1992.
5. Liang, Y.; Shen, J.; Hu, S.; Wang, H.; Pang, J. Effect of TIG current on microstructural and mechanical properties of 6061-T6 aluminium alloy joints by TIG–CMT hybrid welding. *J. Mater. Process. Technol.* **2018**, *255*, 161–174. [CrossRef]
6. Zhang, L.; Li, X.; Nie, Z.; Huang, H.; Sun, J. Softening behavior of a new Al-Zn-Mg-Cu alloy due to TIG welding. *J. Mater. Eng. Perform.* **2016**, *25*, 1870–1879. [CrossRef]
7. Pérez, J.S.; Ambriz, R.R.; López, F.F.C.; Vigueras, D.J. Recovery of mechanical properties of a 6061-T6 aluminum weld by heat treatment after welding. *Metall. Mater. Trans. A* **2016**, *47*, 3412–3422. [CrossRef]
8. Peng, D.; Shen, J.; Tang, Q.; Wu, C.P.; Zhou, Y.B. Effects of aging treatment and heat input on the microstructures and mechanical properties of TIG-welded 6061-T6 alloy joints. *Int. J. Miner. Metall. Mater.* **2013**, *20*, 259–265. [CrossRef]
9. Wang, B.; Xue, S.; Ma, C.; Wang, J.; Lin, Z. Effects of porosity, heat input and post-weld heat treatment on the microstructure and mechanical properties of TIG welded joints of AA6082-T6. *Metals* **2017**, *7*, 463. [CrossRef]
10. Narsimhachary, D.; Bathe, R.N.; Padmanabham, G.; Basu, A. Influence of temperature profile during laser welding of aluminum alloy 6061 T6 on microstructure and mechanical properties. *Mater. Manuf. Process.* **2014**, *29*, 948–953. [CrossRef]
11. Nie, F.; Dong, H.; Chen, S.; Li, P.; Wang, L.; Zhao, Z.; Li, X.; Zhang, H. Microstructure and mechanical properties of pulse MIG welded 6061/A356 aluminum alloy dissimilar butt joints. *J. Mater. Sci. Technol.* **2018**, *34*, 551–560. [CrossRef]
12. Marumoto, K.; Fujinaga, A.; Takahashi, T.; Yamamoto, H.; Yamamoto, M. Selection of Welding Conditions for Achieving Both of High Efficiency and Low Heat Input on Hot-wire GMAW. *J. Manuf. Mater. Process.* **2024**, *8*, 82.
13. Vargas, J.A.; Torres, J.E.; Pacheco, J.A.; Hernandez, R.J. Analysis of heat input effect on the mechanical properties of Al-6061-T6 alloy weld joints. *Mater. Des.* **2013**, *52*, 556–564. [CrossRef]
14. Walter, V.; Weidenmann, K.; Schulze, V. A comparison of FSW, BHLW and TIG joints for Al-Si-Mg alloy (EN AW-6082 T6). *Procedia CIRP* **2014**, *18*, 120–125. [CrossRef]
15. Malin, V. Study of metallurgical phenomena in the HAZ of 6061-T6 aluminum welded joints. *Weld. J. Incl. Weld. Res. Suppl.* **1995**, *74*, 305s–318s.
16. Zhang, K.; Chen, J.; Ma, P.; Zhang, X. Effect of welding thermal cycle on microstructural evolution of Al–Zn–Mg–Cu alloy. *Mater. Sci. Eng. A* **2018**, *717*, 85–94. [CrossRef]

17. Gómora, C.; Ambriz, R.; Curiel, F.; Jaramillo, D. Heat distribution in welds of a 6061-T6 aluminum alloy obtained by modified indirect electric arc. *J. Mater. Process. Technol.* **2017**, *243*, 433–441. [CrossRef]
18. Ambriz, R.R.; Barrera, G.; García, R.; López, V.H. Effect of the weld thermal cycles of the modified indirect electric arc on the mechanical properties of the AA6061-T6 alloy. *Weld. Int.* **2010**, *24*, 321–328. [CrossRef]
19. Tsirkas, S. Numerical simulation of the laser welding process for the prediction of temperature distribution on welded aluminium aircraft components. *Opt. Laser Technol.* **2018**, *100*, 45–56. [CrossRef]
20. Lee, H.T.; Wu, J.L. The effects of peak temperature and cooling rate on the susceptibility to intergranular corrosion of alloy 690 by laser beam and gas tungsten arc welding. *Corros. Sci.* **2009**, *51*, 439–445. [CrossRef]
21. Francis, J.D. Welding Simulations of Aluminum alloy Joints by Finite Element Analysis. Master's Thesis, Virginia Polytechnic Institute, Blacksburg, VA, USA, 2002. Available online: https://vtechworks.lib.vt.edu/server/api/core/bitstreams/de9fb4e3-f86f-4426-9474-9065fbffe0b2/content (accessed on 25 May 2024).
22. Nazemi, N. Identification of the Mechanical Properties in the Heat-Affected Zone of Aluminum Welded Structures. Ph.D. Thesis, University of Windsor, Windsor, ON, Canada, 2015. Available online: https://scholar.uwindsor.ca/etd/5485 (accessed on 9 May 2024).
23. Hu, Y.; Pei, W.; Ji, H.; Yu, R.; Liu, S. Tungsten Inert Gas Welding of 6061-T6 Aluminum Alloy Frame: Finite Element Simulation and Experiment. *Materials* **2024**, *17*, 1039. [CrossRef]
24. Vimalan, D.; Purushothaman, A.; Muthukumaran, S.; Sastikumar, D. Numerical and Experimental Thermal Studies on Friction Welding of AA6061 Plate and AA1060 Tube Using External Tool. *Trans. Indian Inst. Met.* **2024**, *23*, 3184. Available online: https://link.springer.com/article/10.1007/s12666-023-03184-w (accessed on 9 May 2024). [CrossRef]
25. Nélias, D.; Jullien, J.-F.; Deloison, D. Experimental investigation and finite element simulation of laser beam welding induced residual stresses and distortions in thin sheets of AA 6056-T4. *Mater. Sci. Eng. A* **2010**, *527*, 3025–3039.
26. Liang, Z.; Yin, B.; Mo, J.; Wang, S. A new method to deal with the effect of subset size for digital image correlation. *Opt. Int. J. Light Electron Opt.* **2015**, *126*, 4940–4945. [CrossRef]
27. Sutton, M.; Reu, P.L. *International Digital Imaging Correlation Society*; Springer International Publishing: Cham, Switzerland, 2017.
28. Leitão, C.; Galvão, I.; Leal, R.; Rodrigues, D. Determination of local constitutive properties of aluminium friction stir welds using digital image correlation. *Mater. Des.* **2012**, *33*, 69–74. [CrossRef]
29. Lockwood, W.D.; Tomaz, B.; Reynolds, A.P. Mechanical response of friction stir welded AA2024: Experiment and modeling. *Mater. Sci. Eng. A* **2002**, *323*, 348–353. [CrossRef]
30. ESI-Group. *"SYSWELD", Theory Manuals*; ESI-Group: Lyon, France, 2019.
31. GOM. *ARAMIS User Manual–Software*; GOM GmBH: Braunschweig, Germany, 2016.
32. Niu, L.-Q.; Li, X.-Y.; Zhang, L.; Liang, X.-B.; Li, M. Correlation Between Microstructure and Mechanical Properties of 2219-T8 Aluminum Alloy Joints by VPTIG Welding. *Acta Metall. Sin.* **2017**, *30*, 438–446. [CrossRef]
33. ASM International. *Casting Handbook*; ASM International: Materials Park, OH, USA, 2008; Volume 15, pp. 416–522.
34. Myhr, O.; Grong, Ø.; Fjær, H.; Marioara, C. Modelling of the microstructure and strength evolution in Al–Mg–Si alloys during multistage thermal processing. *Acta Mater.* **2004**, *52*, 4997–5008. [CrossRef]
35. Hirose, A.; Kurosawa, N.; Kobayashi, K.F.; Todaka, H.; Yamaoka, H. Quantitative evaluation of softened regions in weld heat-affected zones of 6061-T6 aluminum alloy—Characterizing of the laser beam welding process. *Metall. Mater. Trans. A* **1999**, *30*, 2115–2120. [CrossRef]
36. Maisonnette, D.; Suery, M.; Nelias, D.; Chaudet, P.; Epicier, T. Effects of heat treatments on the microstructure and mechanical properties of a 6061 aluminium alloy. *Mater. Sci. Eng. A* **2011**, *528*, 2718–2724. [CrossRef]